Design and performance analysis of a High Field Side antenna for Plasma Position Reflectometry control on DTT

J.M. Santos, A. Silva, F. da Silva, Y. Nietiadi, R. Luís, J. Ferreira, G. de Masi, O. Tudisco, R. Cavazzana, P.R. Resende, et al.

Design and Performance analysis of a High Field Side antenna for Plasma Position Reflectometry control on DTT

J. M. Santos[a], A. Silva[a], F. da Silva[a], Y. Nietiadi[a], R. Luís[a], J. Ferreira[a], G. De Masi[b], O. Tudisco[b], R. Cavazzana[b], P. R. Resende[d], J. C. C. Abrantes[d], S. Heuraux[e], E. Ricardo[a], T. Ribeiro[f]

[a]*Instituto de Plasmas e Fusão Nuclear, Instituto Superior Técnico, Universidade de Lisboa, 1049-001 Lisboa, Portugal*
[b]*Consorzio RFX, C.so Stati Uniti, 35127 Padova, Italy*
[c]*Associazione EURATOM-ENEA-CR Frascati, 00044 Frascati, Italy*
[d]*proMetheus, Instituto Politécnico de Viana do Castelo,4900-348 Viana do Castelo, Portugal*
[e]*Institut Jean Lamour, Université de Lorraine, CNRS, F-54000 Nancy, France*
[f]*Max-Planck-Institut für Plasmaphysik, Garching D-85748, Germany*

The Divertor Test Tokamak (DTT) will allow the test and validation, in reactor-like regimes, of control diagnostics relevant to DEMO operation. In DEMO, Plasma Position Reflectometry (PPR) will provide non-magnetic measurements of plasma position and shape, involving the use of several poloidally distributed lines-of-sight (LOS). A multi-LOS PPR is presently under design on DTT to gather more experimental knowledge on the operation of such systems out of the usual equatorial plane LOS. Priority has been given to planning the High-field-side (HFS) reflectometers due to their impact on the design of the first wall and vessel. To cope with the severe space and access constraints imposed to the antenna placement on the inner side of the tokamak vessel, two optimized, small-footprint, bistatic and monostatic hog-horn antenna designs are proposed. To demonstrate the viability of a PPR implementation on DTT's HFS, we present herein 3D full-wave simulations in the DTT single null plasma scenario, laboratory measurements of a 3D-printed bistatic antenna prototype, and a preliminary thermal analysis of the antenna when embedded in the plasma-facing wall structures under standard plasma operation conditions.

Keywords: Antenna design, FDTD full-wave simulations, Plasma Position Reflectometry, Plasma facing component thermal analysis, DTT, DEMO.

1. Introduction

The Divertor Test Tokamak (DTT) [1], designed to test advanced alternative power exhaust solutions, offers the added possibility of testing and validating, in reactor-like regimes, relevant non-magnetic control diagnostics in support of the DEMO design. One such diagnostic, O-mode reflectometry, was proposed as an alternative source of real-time (RT) plasma position and shape measurements for control purposes. At DEMO, Plasma Position Reflectometry (PPR) involves the use of several poloidally distributed lines-of-sight (LOS). However, since on present devices profile reflectometers are mainly built at the equatorial plane, experience in PPR control has only been gained by probing the plasma at this plane, simultaneously both from the Low and High Field Sides (HFS) [2][3]. To gather more comprehensible experimental knowledge on the operation of such systems, before a full deployment on DEMO, a multiple LOS PPR in DTT is presently under consideration. Priority has been given to planning the HFS reflectometer system due to its impact on the design of the first wall components and vacuum vessel. Herein we investigate two optimized, small-footprint, bistatic and monostatic hog-horn antennas designed to cope with the severe constraints imposed on the HFS antennas' size, access to the chamber, and in-vessel waveguide routing (section 2). The proposed antennas' measurement performance is assessed in the DTT single null (SN) scenario (as defined in [4]) using 3D Finite-Difference Time-Domain (FDTD) codes of the REFMUL family [5] (section 3). The simulation results are further complemented by laboratory tests of a 3D-printed metal mockup of the bistatic antenna (section 4). Finally, CAD models of the bistatic antenna, embedded in a preliminary model of the inboard first wall, were used to produce a first thermal analysis (section 5) to be discussed in the frame of the proposed HFS antennas' viability assessment. This exercise is the first application of an integrated design workflow that incorporates reflectometry 3D advanced full-wave simulations and thermal analysis in the iterative development cycle of a PPR system.

2. Antenna designs

The design of the HFS PPR antennas presented in this paper was driven and constrained by the evolving design of the DTT's inboard first wall (FW). To enable a realistic antenna performance analysis at this early stage, they were originally designed to be accommodated in the inner limiter modules, along one of the cooling pipes. In the simulations, to protect the exposed antenna block face from the plasma, one of these limiter submodules was recessed 1 cm (bottom left drawing of Fig. 3). This reduced the space available between the plasma-facing protective tiles and the vacuum vessel inner shell to a

author's email: jorge.santos@ipfn.tecnico.ulisboa.pt

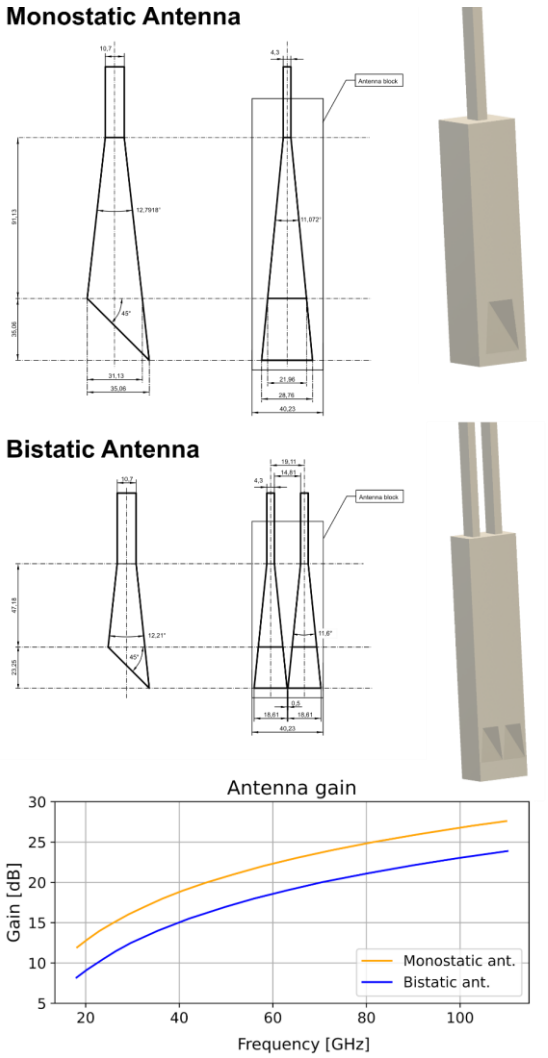

Fig. 1 – Dimensions and 3D renders of the designed monostatic and bistatic antenna blocks and respective antenna gain curves.

~41.5mm×51mm (W×D) footprint. No constraints were imposed on the length of the antennas' block along the submodule. Additionally, each antenna should accommodate microwave K, Ka, Q, V and W bands (18 to 110 GHz), to give access to and above separatrix densities (~9.6×10^{19} m^{-3} for the SN scenario) and be fed by standard WR42 K band waveguides. Under these constraints, only hog-horn type antennas with flat mirrors can be used to simultaneously accommodate all bands and produce a probing beam perpendicular to the waveguide reaching the antenna block. The waveguides, routed through the narrow space behind the plasma facing tiles, reach the antenna from above (top ports) to avoid the recollection of any particles resulting from plasma operation. This implies using different cooling pipes in the HFS FW module to accommodate different PPR LOS. To address these stringent requirements, two antenna blocks were proposed housing either i) a bigger monostatic antenna or ii) two side-by-side smaller antennas, in a bistatic arrangement as seen in Fig. 1. A bigger monostatic antenna has the advantage of a bigger gain and of requiring the routing of only one waveguide, shared between emitted and reflected waves, behind the FW components. However, because all bands share the

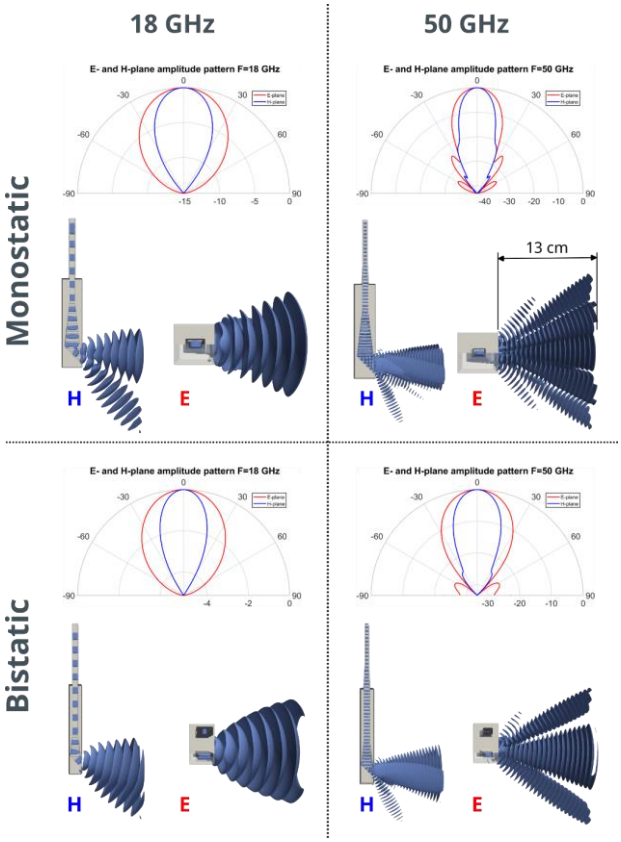

Fig. 2 - Antenna radiation patterns in the E- and H-Planes for 18 and 50 GHz: Far field polar plots (top) and corresponding simulated (REFMUL3) beam propagation in vacuum in the near field (bottom).

same antenna and return path, no schemes with directional couplers to separate emitted and received waves close to the antenna are feasible (as implemented in the ASDEX Upgrade HFS multi-antenna reflectometer [6]). This results in the detection of the fainter plasma reflection mixed with spurious higher-powered reflections of the emitted wave inside the long waveguide, in particular at the vacuum windows placed in the vessel's vacuum boundary. For this reason, the bistatic antenna, albeit of lower gain (~ -3 dB, Fig. 1 bottom plot) and with an offset axis of emission (Tx) and reception (Rx), can prove to be a better choice as it allows the detection of the reflected waves separate from any such corruptions. Furthermore, by duplicating the backend microwave electronics, such an antenna can still provide a simultaneous monostatic and bistatic operation with the same placement/routing requirements.

Fig. 2 shows the polar plots of the calculated E- and H-plane far-field radiation patterns, for both antennas, for 18 GHz (first K band frequency) and 50 GHz (last Q band frequency) frequencies. The 3D views shown therein depict the radiated beams in the near field in the same planes. The later were obtained using the REFMUL3 full-wave code in the region where the plasma measurements will take place, as we will see in more detail in section 3. As can be seen, and specially for lower frequencies, the simulation patters exhibit an asymmetric downfacing secondary lobe, due to wave diffraction in the bottom mirror lip, that is not captured by the far-field raytracing calculation. Due to its smaller dimensions, the bistatic

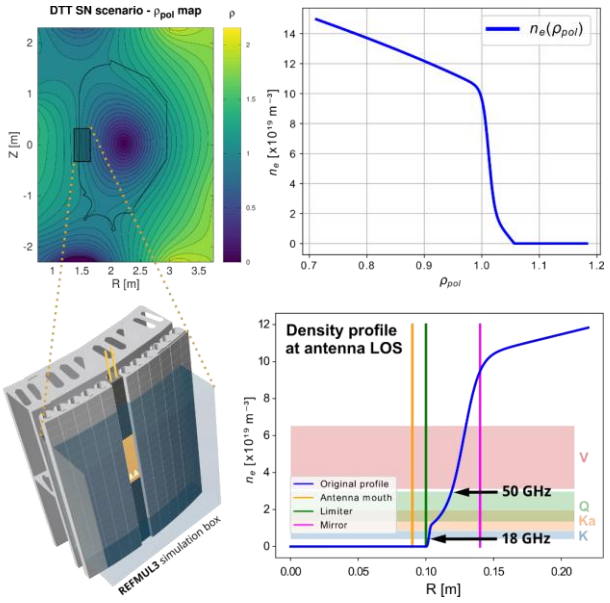

Fig. 3 – Density profile and magnetic equilibrium of DTT SN low gas puffing reference scenario (top plots). Representation of the bistatic antenna embedded in the FW structure and of the REFMUL3 simulation box (bottom left). Profile taken from the simulation box in the emitting antenna's LOS.

antenna far field, where the wave front is flatter, is attained closer to the antenna when compared to the bigger monostatic one (far field $\geq (2D^2)/\lambda$ where D is the antenna's mouth largest dimension). This means that cutoff layers of higher densities and, hence increased distance from the antenna (albeit still in the close proximity of the antenna) will be reached in better propagation and reflection conditions.

3. Antenna performance analysis

3.1 REFMUL3 simulation setup

The performance validation of the microwave diagnostic in the PPR application presented herein makes use of the REFMUL3 3D FDTD full-wave code [7] and of its ability to import full CAD designs into the simulations[8]. This code allows a realistic simulation that fully incorporates the essential 3D effects that affect wave propagation in the plasma, and its interaction with the instrument's launching and receiving antennas, as well as with the surrounding FW plasma facing components. PPR diagnostics aim at providing the tokamak control systems with measurements of the plasma position and shape within an accuracy of ± 1 cm. This accuracy needs to be achieved at the separatrix, the last closed magnetic surface that defines the plasma shape and is usually used for this type of plasma control. Herein we assess the position errors incurred in the standard reflectometry density profile reconstruction in the flat-top of the SN plasma scenario with low gas puffing (reference scenario, $I_p = 5.5$ MA, $B_T = 6.6$ T, and 1.6×10^{20} m^{-3} of core electron density), as defined by the profile in the top right plot of Fig. 3. The top left plot shows the SN scenario equilibrium used to generate, from this profile, the 3D plasma volume used in the simulation [9]. The bottom right plot shows the profile mapped to the HFS, at the antenna's LOS, in simulation box coordinates. We simulated the antenna measurements at the DTT equatorial plane using a 22×45×50 cm simulation box that encompasses the antenna block, FW components, and the ~12 cm radial extent in which the relevant plasma cutoff density layers stand (K-V band coverage, see Fig. 3 bottom plots). This corresponds to 3D simulation boxes with sizes ranging from 396×10^6 points (K band) up to ~6.1×10^9 points (V band). Each band's full frequency sweep simulation took between ~1.5 h (K) and 24 h (V) to run on 64 nodes (3072 cores) on Marconi supercomputer [10]. Simulations were performed with and without FW to single out the influence of the surrounding plasma facing structures on the reflectometry measurement. For both cases, simulations were made i) in vacuum to determine the near-field antenna radiation patterns, ii) in vacuum with a mirror placed at 5 cm to calibrate the measurements for any dispersive effects affecting propagation inside the short waveguide stretches and to radially reference the density profiles to the antenna mouth, and iii) in the SN reference plasma.

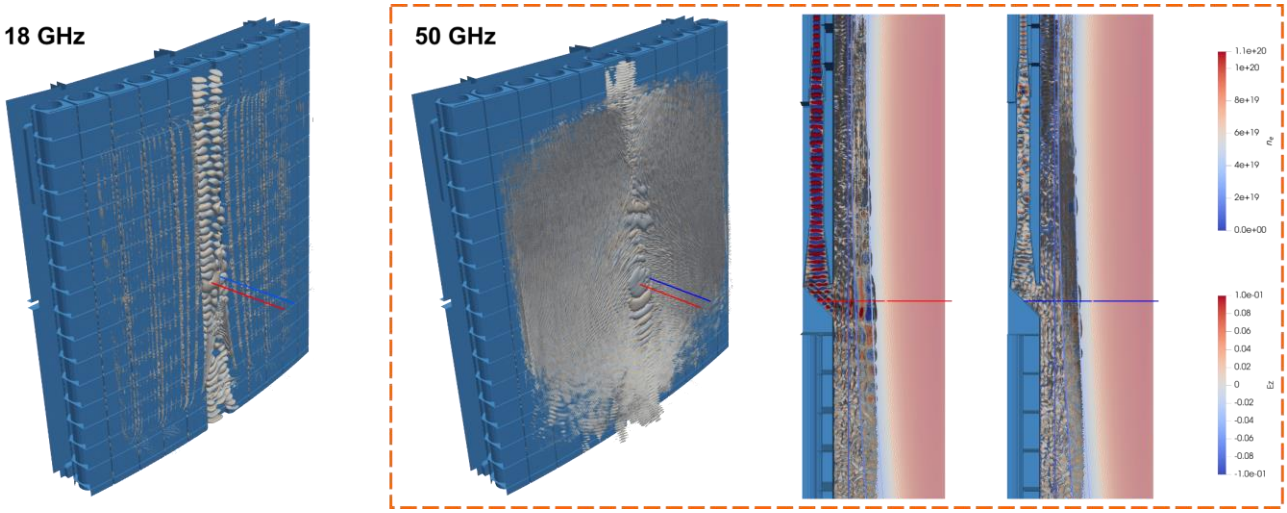

Fig. 4 – Full band frequency swept REFMUL3 simulations of the bistatic antenna (emitting LOS in red and receiving in blue). Snapshots taken at 18GHz (beginning of K band) and 50 GHz (end of Q band). Poloidal cut views of the propagated electric field at the emission and receiving planes (right graphs, left-to-right order, respectively).

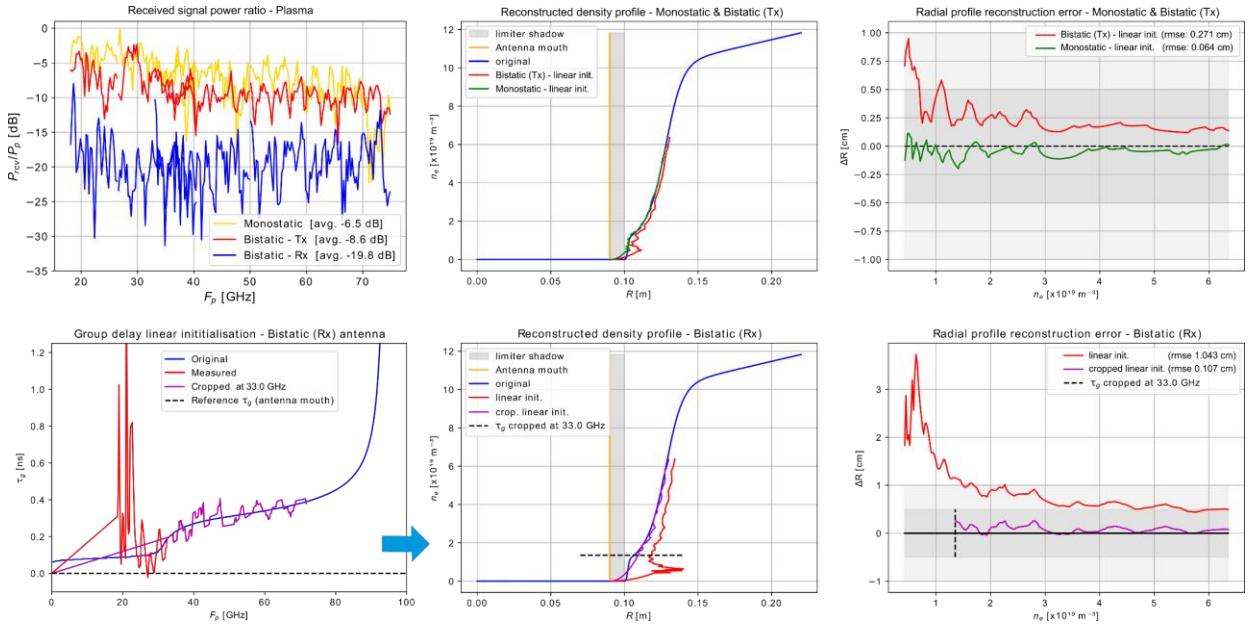

Fig. 5 – Transfer of power between antennas in the presence of plasma (top left); profiles and profile reconstruction errors using both antennas in monostatic mode (two top rightmost plots); linearly initialized group delay measured with signal received by the receiving (Rx) bistatic antenna (bottom left plot), and corresponding profiles and reconstruction error curves (two bottom rightmost plots).

3.2 Performance analysis – full-wave simulations

In Fig. 4 the 3D figures and 2D poloidal plane slices (right) show snapshots of K and Q band full sweep simulations of the bistatic antenna in the reference SN plasma. The visualized wave fronts are reflecting at 0.4×10^{19} m^{-3} (18 GHz) and 3.1×10^{19} m^{-3} density layers (refer to the bottom density profile in Fig.3). In the former case, waves get reflected just ~1 cm from the antenna, at the limiter position, where a very steep density gradient exists roughly between 0 and 1.2×10^{19} m^{-3}. Reflected waves bounce back and forth all along the channel formed by the recessed limiter submodule and the reflecting plasma layer at the FW limiter tiles. In the latter case, the density cutoff layer is ~3 cm from the antenna (2 from the limiter wall), and the waves penetrate deeper in the front facing plasma. The waves are no longer just trapped along the recessed submodule, also reflecting back and forth in the FW tiles in the vicinity of the antenna block. The red and blue lines show the LOS of both emitting (Tx) and receiving (Rx) antennas respectively. The beam spot at the reflecting layer is visibly centered around the Tx LOS and therefore the energy of the returning waves along the offset Rx LOS is lower, as can be seen in the slices of the electric field taken at both LOS (right side of Fig 4). This observation is corroborated by the measurements of the ratio between the received signal power and the emitted signal power (top left plot of Fig. 5). As expected, the monostatic antenna (yellow curve), with higher gain and centered in the recessed FW submodule, captures a bigger fraction of the emitted energy, ~2 dB higher than the captured by the bistatic emitting antenna (red). This power ratio naturally decreases with the increasing distance to the higher density reflecting layers (higher probing frequencies). The energy received by the off-centered bistatic Rx antenna (blue) is on average ~11 dB below its Tx counterpart.

The received signal (electric field at the center of the antennas Tx or Rx waveguide) is mixed with an in-phase and quadrature (IQ) reference chirp signal. This generates an interference signal from which the low frequency component, related to the phase variations due to the propagation in the plasma up to the reflecting layer and back, is obtained by low pass filtering. The group delay of the waves propagating in the plasma is calculated [11],[12] from the beat frequency evolution, extracted from interference signal using standard sliding Fourier techniques. Because the plasma is probed only for frequencies above 18 GHz (for densities above 0.4×10^{19} m^{-3}) the group delay measurement below this first probing frequency needs to be initialized with an educated guess. In the ASDEX Upgrade, where PPR plasma position control has been successfully demonstrated [2], HFS group delay measurements are usually automatically initialized using a linear interpolation between 0 (corresponding to the antenna mouth radial position) and the first group delay measured, resulting in a parabolic profile below the first probed density. The density profile is then obtained by Abel inversion of the initialized group delay curve. Provided the distance from the antenna to the first probed reflecting layer is short (few centimeters) and the first evaluated group delay values are not very noisy, such a simple initialization guess will not result in a large profile reconstruction error. When applying the same processing techniques to the signals obtained from the simulations, it can be seen that this is mainly the case of the measurements made with the monostatic and bistatic Tx antennas (top two rightmost plots of Fig. 5). Although in the bistatic Tx case the group delay exhibits a noisier evolution in the first two bands, the profile reconstruction errors remain well below 1 cm, with an RMS error of 2.71 mm. The non-centered emission of the probing waves with respect to the recessed channel in which the antenna is embedded, aggravated by the bigger curvature of the waves in the antenna's near-field, seems to be the culprit for the noisier measurements at the lower probing frequency range (K and Ka bands). This contrasts with the cleaner monostatic antenna measurement that resulted in a profile reconstruction with a 0.64 mm RMS error. In the case of the bistatic Rx antenna, to the mentioned effects

we need to add a reception LOS that is offset from the emission's LOS. The result is a lower power received signal, more affected by the reflected wave's multiple return paths and their reflection inside the recessed volume surrounding the antenna mouth. The three lower plots of Fig. 5 show the resulting noisier group delay, and the corresponding inverted profile and reconstruction error (red curves, from left to right). In the K-Ka frequency range below 33 GHz, the group delay is highly affected with a deviation to the actual profile's group delay (in blue) that reaches an order of magnitude. The automatic linear initialization to such values further aggravates the initialization errors propagated through the profile. However, as the density profile is already detached from the wall above 1.3×10^{19} m^{-3} (33 GHz – first frequency of Q band), the group delay measurement becomes less noisy. If only Q and V band data is used (magenta curves), the reconstructed profile, even with such a simple/blind initialization procedure, returns very low density profile reconstruction errors with the RMS error dropping from 1.043 cm to 1.07 mm. Nevertheless, in all presented cases, the PPR 1 cm accuracy requirement is widely satisfied at the target separatrix densities (~9.6×10^{19} m^{-3} for the SN scenario).

It must be noted that these simulations were performed in a non-perturbed, turbulence free plasma. The existence of density fluctuations would contribute to noisier group delay measurements that, in turn, would result in worse reconstruction errors. Although these simulations already give hints on the expected performance of the present design of the proposed antennas, and on the need to use more sophisticated algorithms to improve the measurements reliability/accuracy (particularly in the case of the bistatic antenna), they do not incorporate the effects of the reflections along the long transmission lines that might hamper the use of both antennas in monostatic mode. This is why the possibility of operating the bistatic antenna in a hybrid mode (bistatic and monostatic modes) might make it a safer choice over the higher gain monostatic one. Additionally, in the foreseen higher gas puffing SN scenarios the early steep density gradient region extends to much higher densities, hiding inverted density gradients (dip in the density profile) that require the use of specific profile reconstruction techniques presently under investigation [13]. These advanced 3D simulations are being used to address some of these issues, and their outcome is being gradually incorporated into the iterative design process of the PPR antennas.

4. Bistatic antenna laboratory tests

To evaluate the real world performance of the bistatic antenna and, at the same time, validate the REFMUL3 code, a 3D printed prototype in maraging steel was manufactured at the *proMetheus* Lab by Direct Metal Laser Sintering on a TRUMPF TruPrint 1000 printer (layer thickness $< 20\ \mu m$, and measured average surface roughness of $Ra \cong 7.2\ \mu m$ [14]).

A set of laboratory electromagnetic tests were then performed to measure the following parameters:

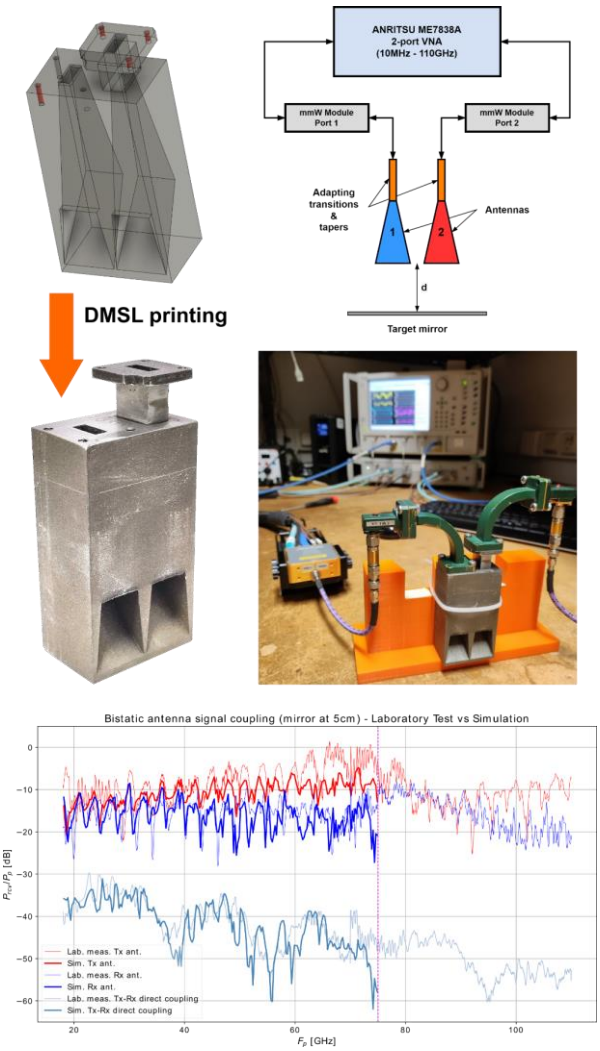

Fig. 6 - Adapted bistatic CAD model and DMSL printed prototype (left top and center), experimental test setup (right top and center), simulation versus laboratory measurements of signal coupling (bottom).

- **Antenna coupling** – The transfer of power through space between antennas in the presence of a reflecting metallic mirror (equal to the ratio of the power received by one antenna, to the power radiated by the other or by itself).
- **Antenna crosstalk** – The unwanted transfer of power through space between antennas looking to free space or to a microwave absorbing material wall (equal to the ratio of the power received by one antenna to the power radiated by the other).
- **Antenna VSWR** (Voltage Standing Wave Ratio) – a measure that describes numerically how well the antenna is impedance-matched to the transmission line it is connected to.

The tests were performed in the 18 – 110 GHz frequency range using five standard millimeter wave bands (K, Ka, Q, V and W). Fig. 7 top right diagram shows the experimental setup used for the tests. A vector network analyzer (VNA) was used both to sweep the frequency of the input signal and to perform the (heterodyne) detection of the reflected signals, together with a combination of different waveguide transitions and tapers to match the different frequency bands. A metallic mirror was placed

at different known distances to measure the antenna coupling. For each position of the target mirror, we measured the four parameters of the Scattering (S)-matrix: S_{11} and S_{22}, correspond to the monostatic measurements performed by each antenna, and S_{12} and S_{21}, correspond to the bistatic measurements performed by alternating the emission and reception antennas. From S_{11} and S_{22} acquired with the mirror in place, the monostatic antenna coupling is measured. While the coupling between antennas 1 and 2 (bistatic) is measured from S_{12} and S_{21}. The mirror was then removed from the front of the antenna to measure its crosstalk and VSWR. Without mirror, S_{12} and S_{21} are used to measure the antennas' 1 and 2 crosstalk. De-embedding was performed in all measured S parameters to remove test setup fixture characteristics (transitions, tapers, cables, etc.) from the measured results and to improve accuracy. The results show a good coupling between antennas 1 and 2 (target reflection) and the capability of operating in a monostatic configuration with improved performance for short probing range. The measured S_{12}/S_{21} show that crosstalk between antennas 1 and 2 is below -30 dB and S_{11}/S_{22} show an average value of -16.4 dB which by applying $VSWR = (1 + |S_{nn}|) / (1 - |S_{nn}|)$ leads to an average VSWR of 1.36, revealing a good antenna impedance matching.

Table 1. Received signal power ratio average value (P_{RCV}/P_P).

Measurement	Lab. meas. (< 75 GHz)	REFMUL3 simulation
Direct coupling (no mirror/S12/simTx-Rx)	-40.9 dB	-41.1 dB
Monostatic (mirror/S11/sim Tx)	-8.4 dB	-12.0 dB
Bistatic (mirror/S12/sim Rx)	-15.3 dB	-16.1 dB

The results obtained for a mirror placed at 5 cm of the antenna mouth (bottom plot of Fig. 7 and table 1) show a very good qualitative and quantitative (< 5% for direct bistatic coupling) agreement between the laboratory measurements and REFMUL3 code's data, being an outstanding validation of the simulation code. No antenna radiation patterns were measured due to the unavailability of an anechoic chamber at the time the laboratory tests were performed.

5. Bistatic antenna thermal analysis

The plasma-facing antennas in DTT are expected to operate under high thermal loads. Therefore, as previously done for ITER [15] and DEMO [16], a preliminary thermal analysis is important to estimate the involved operating temperatures and to evaluate eventual cooling needs for the antenna block under consideration. This first analysis, performed using ANSYS Mechanical and CFX [17], is summarized in Fig. 7. After the initial REFMUL3 simulations were performed, it was decided that the antenna block should be embedded in a standard module FW section (Fig. 7 top left drawing), after the removal of a segment of the central cooling pipe. As a result, no water circulates in the central pipe, which means

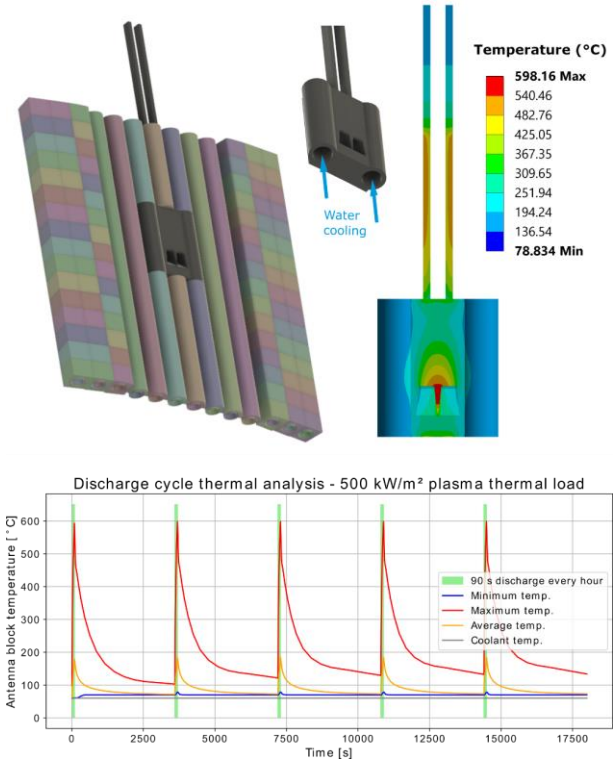

Fig. 7 - Preliminary thermal analysis (top right) of a cooled bistatic antenna block embedded in the current FW standard module configuration (top left) during continued DTT operation (bottom).

that the only cooling available to the antennas comes from the adjacent pipes. This is a conservative assumption, since in practice the design of the cooling system will have to be adapted to accommodate the antenna block. For DTT, the nuclear loads in the first wall were previously estimated to remain below ~10 mW/cm^3 [18], almost one order of magnitude lower than the volumetric loads expected for ITER [19]. For the plasma thermal loads, ~0.5 MW/m^2 are expected at the first wall, as estimated in [1, p. 166]. These values were assumed as boundary conditions: the nuclear load was added as internal heat generation in the full antenna block, while the thermal load was applied to all the plasma-facing surfaces. Cooling water was assumed to enter the pipes at 60 °C. With these assumptions, a transient thermal analysis was performed assuming 90-second plasma pulses with 1 hour between pulses [1, p. 102]. It can be seen in Figure 7 that this discharge cycle is long enough to allow the temperatures to stabilize between pulses. A maximum value of 598 °C was obtained in the thin surface between the Tx and Rx antennas (with much lower temperatures elsewhere). This is above the limits foreseen for stainless steel under neutron irradiation in ITER (450 °C) [15] and DEMO (550 °C) [16]. To remove this hotspot, a more efficient cooling system design is required to bring the cooling water closer to the antenna axis.

6. Conclusions

This exercise is the first application of an integrated design workflow for a PPR diagnostic system. The workflow uses common CAD models of antenna and first-wall components, incorporates 3D advanced full-wave simulations in target plasma scenarios, and includes

laboratory tests of laser metal printed prototypes and thermal analysis of plasma facing components in the iterative development cycle. The highly restricted dimensions imposed on the HFS PPR antennas resulted in non-optimal solutions from the perspective of the antenna performance. However, their performance was assessed by 3D full-wave FDTD simulations both in vacuum and with plasma. The former were compared with laboratory tests of a 3D printed mockup of the most desirable bistatic design, attesting the very high degree of realism and absolute accuracy achievable with the synthetic diagnostic based on the REFMUL3 simulator. The latter allowed to have an insight of the interplay between the probing waves, the FW in which the antennas are embedded, and the plasma. It was shown that in all the designs, and in particular above densities of $n_e \approx 1.5\times10^{19}$ m^{-3}, density layer location accuracy satisfied the $\Delta R<1$ cm PPR requirement, validating the tested antenna/first wall configurations. From the simulation results, the lower gain bistatic antenna seems to be the design choice to pursue as it allows simultaneously monostatic and full bistatic operation. When compared to the monostatic antenna, the bistatic in monostatic operation (Bistatic - Tx), albeit with a lower (~3 dB) gain performs almost as well. In full bistatic operation (Bistatic -Rx) the antenna allows the separation of the reflected wave in a waveguide route free from any high-powered parasitic reflections in the long emission waveguide path common to all bands being probed. It was shown that in this case the recovery of good measurements in the lower K and Ka bands is challenging, requiring a redesign of the antenna or first wall embedding, and/or more advanced data processing techniques to extract the group delay measurements from the detected signals. The thermal analysis of a cooled antenna block built around the bistatic antenna also shown the need to further iterate its design. Better cooling or the use of e.g. tungsten coating will be needed to remove the identified hotspot under normal DTT operation. We have shown the benefits of a comprehensive and integrated design flow aimed to ensure that a final design for the PPR antenna setup can be reached with a maximized probability of operational success. This design work will be pursued soon with updated CAD models of the integration of iterated antennas in current and future first wall designs.

Acknowledgments

IPFN activities received financial support from “Fundação para a Ciência e Tecnologia” through projects UIDB/50010/2020 and UIDP/50010/2020. This work has been carried out within the framework of the EUROfusion Consortium, funded by the European Union via the Euratom Research and Training Programme (Grant Agreement No. 101052200—EUROfusion) and under the EUROfusion Enabling Research project ENR-TEC.01.IST and HPC Project CfP-FSD-AWP23-AC-01-IST-06. Views and opinions expressed are, however, those of the author(s) only and do not necessarily reflect those of the European Union or the European Commission. Neither the European Union nor the European Commission can be held responsible for them.

References

[1] R. Martone et al. DTT Divertor Tokamak Test facility–Interim Design Report., ENEA (2019) https://iris.enea.it/handle/20.500.12079/54983.

[2] J. Santos et al. Reflectometry-based plasma position feedback control demonstration at ASDEX Upgrade, Nucl. Fusion 52 (3) (2012) 032003

[3] J. M. Santos et al. Real-time reflectometry – an ASDEX Upgrade DCS plugin App for plasma position and shape feedback control, Fusion Eng. Des. 123 (2017) 593

[4] F. da Silva et al. Assessment of measurement performance for a low field side IDTT plasma position reflectometry system, Fusion Eng. Des. 168 (2021) 112405

[5] F. da Silva et al. Benchmarking 2D against 3D FDTD codes for the assessment of the measurement performance of a low field side plasma position reflectometer applicable to IDTT, JINST 17 (2022) C01017

[6] A. Silva et al. Ultrafast broadband frequency modulation of a continuous wave reflectometry system to measure density profiles on ASDEX Upgrade., Rev. of Sci. Instr., 67(12) (1996) 4138–4145

[7] R. Hatzky, HLST Core Team Report, EUROFUSION WPISA-REP (18) (2017) 20587.

[8] J. M. Santos et al. A 3D CAD model input pipeline for REFMUL3 full-wave FDTD 3D simulator, JINST 16 (2021) C11013

[9] E. Ricardo et al. Simulation and data processing techniques to design optimized PPR systems on plasma fusion devices, Comp. Phys. Com. 294 (2024)108945

[10] https://www.hpc.cineca.it/hardware/marconi

[11] J. Santos, Fast reconstruction of reflectometry density profiles on asdex upgrade for plasma position feedback purposes, Ph.D. thesis, Technical University of Lisbon (2008)

[12] E. Mazzucato, Microwave reflectometry for magnetically confined plasmas, Review of Scientific Instruments 69 (6) (1998) 2201

[13] R. B. Morales et al. Reconstruction of hollow areas in density profiles from frequency swept reflectometry, Plasma Sci. Technol. 22 (2020) 064005

[14] C. M. A. Vasques et al. Quality Analysis of a 3D-Printed Maraging Steel Part, Proc. of the ASEC2021 - 2nd International Electronic Conference on Applied Sciences, 15–31 Oct 2021, https://sciforum.net/paper/view/11177

[15] Y. Nietiadi et al. Thermal analyses of the in-vessel frontends of the ITER plasma position reflectometry system Fus. Eng. Des. 156 (2020) 111599

[16] Y. Nietiadi et al. Nuclear and thermal analysis of a multi-reflectometer system for DEMO, Fus. Eng. Des. 167 (2021) 112349

[17] ANSYS®Academic Research Mechanical, Release 2023

[18] R. Villari et al, Nuclear design of Divertor Tokamak Test (DTT) facility, Fus. Eng. Des. 155 (2020) 111551

[19] R. Luís et al. Neutronics Analysis of the In-Vessel Components of the ITER Plasma-Position Reflectometry System on the High-Field Side, IEEE Trans. Nucl. Sci. 65-9 (2018) 2404-2411